Nanodome Solar Cells with Efficient Light Management and Self-Cleaning

Jia Zhu,[†] Ching-Mei Hsu,[‡] Zongfu Yu,[§] Shanhui Fan,[†] and Yi Cui*,[‡]

[†]Department of Electrical Engineering, [‡]Department of Materials Science and Engineering, and [§]Department of Applied Physics, Stanford University, Stanford, California 94305

ABSTRACT Here for the first time, we demonstrate novel nanodome solar cells, which have periodic nanoscale modulation for all layers from the bottom substrate, through the active absorber to the top transparent contact. These devices combine many nanophotonic effects to both efficiently reduce reflection and enhance absorption over a broad spectral range. Nanodome solar cells with only a 280 nm thick hydrogenated amorphous silicon (a-Si:H) layer can absorb 94% of the light with wavelengths of 400−800 nm, significantly higher than the 65% absorption of flat film devices. Because of the nearly complete absorption, a very large short-circuit current of 17.5 mA/cm^2 is achieved in our nanodome devices. Excitingly, the light management effects remain efficient over a wide range of incident angles, favorable for real environments with significant diffuse sunlight. We demonstrate nanodome devices with a power efficiency of 5.9%, which is 25% higher than the flat film control. The nanodome structure is not in principle limited to any specific material system and its fabrication is compatible with most solar manufacturing; hence it opens up exciting opportunities for a variety of photovoltaic devices to further improve performance, reduce materials usage, and relieve elemental abundance limitations. Lastly, our nanodome devices when modified with hydrophobic molecules present a nearly superhydrophobic surface and thus enable self-cleaning solar cells.

KEYWORDS Nanocone, nanodome, solar cell, light trapping, photovoltaics

Solar cells of nanostructures such as nanocrystals and nanowires have attracted much attention due to their potential for improving charge collection efficiency, fabricating small-scale power sources, enabling novel conversion mechanisms, and using low-cost processes.[1−6] Efficient light management by reducing incident light reflection while enhancing optical absorption is important for all photovoltaic devices for performance improvement and cost reduction.[7,8] Even though nanostructure-based graded refractive index[9−15] and plasmonic[7,16−21] layers offer great potential for antireflection coating and absorption enhancement, respectively, they are mostly limited to use as an additional coating on active solar absorber surfaces.

We have chosen p-i-n a-Si:H solar cells to demonstrate the nanodome concept. a-Si:H is one of the most important photovoltaic systems, as it is based on abundant, nontoxic materials, and low temperature processes.[22−24] a-Si:H can absorb light very efficiently, with an absorption depth of only 1 μm (at around 1.8 eV), several hundred times thinner than that of crystalline silicon. Previously we have demonstrated that a-Si:H nanocones with lengths close to the absorption depth have antireflection properties for a wide range of wavelengths and angles of incidence without any extra antireflection coating.[13] However, carriers of a-Si:H have very poor transport properties, especially their short carrier diffusion length of around 300 nm or less. In addition, the 10−30% efficiency degradation under light soaking, known
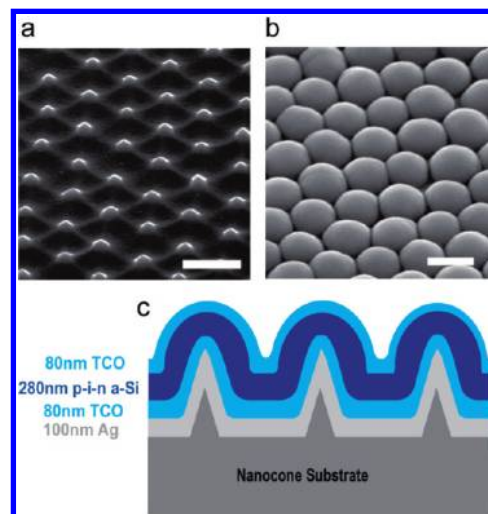

FIGURE 1. Nanodome a-Si:H solar cell structure. SEM images taken at 45° on (a) nanocone quartz substrate and (b) a-Si:H nanodome solar cells after deposition of multilayers of materials on nanocones. Scale bar 500 nm. (c) Schematic showing the cross-sectional structure of nanodome solar cells.

as the Stabler−Wronski effect, is found to be less severe with thinner films (below 300 nm).[22−24] Hence efficient light harvesting within a much thinner layer (<300 nm) is essential to the device performance of this type of solar cell.

Our typical single p-i-n junction nanodome a-Si:H solar cells consist of 100 nm thick Ag as a back reflector, 80 nm thick transparent conducting oxide (TCO) as both bottom and top electrode, and a thin a-Si:H active layer of 280 nm (from top to bottom: p-i-n, 10−250−20 nm) (Figure 1c). Nanodome solar cells were fabricated on nanocone sub-

strates (Figure 1a). Nanocone glass or quartz substrates were first fabricated by Langmuir—Blodgett assembly of close packed monodisperse SiO₂ nanoparticles followed by reactive ion etching developed in our group (see Methods).[13,25] The base diameters and spacings of nanocones can be controlled in the range of 100—1000 nm, which is relevant to the sunlight wavelengths. Nanocones with a base diameter of 100 nm, spacing of 450 nm and height of 150 nm are reported in this study (Figure 1a). The solar cell layers were conformally deposited on top of the nanocone substrate as well as on a flat substrate for comparison. After deposition, the nanocone pattern is largely transferred to the top layer although nanocones become nanodomes, as shown in scanning electron microscopy (SEM) images (Figure 1b).

To characterize the effect of antireflection and light trapping on these nanodome solar cells, we have conducted standard hemispherical absorption measurements with an integrating sphere. The absorption measurement was carried out over a broad wavelength range (400—800 nm), which covers most of the spectrum that is useful for a-Si:H with a band gap of 1.75 eV (or ∼710 nm), although a-Si:H has a long band tail. For comparison, flat a-Si:H film solar cells with the same layer thickness were also measured. Since TCO has a lower refractive index (2.2) than that of a-Si:H (∼4.23), measurements were also carried out with and without the top TCO layer for both types of solar cells. The absorption data in the wavelength range of 400—800 nm under normal incidence are summarized in Figure 2a. Green and black curves are from nanodome devices with and without the top TCO layers while blue and red ones are from flat film devices with and without the top TCO layers, respectively. The weighted absorption, integrated over the whole spectrum under the 1 Sun AM 1.5 illumination condition, is plotted in Figure 2f.

There are several important observations from these data. First, nanodome devices show significantly larger absorption than flat film devices over the whole spectrum. Nanodomes with a top TCO layer show extremely high total weighted absorption of 94 % while flat films with a top TCO layer only show 65 % (Figure 2f).

Second, the absorption of nanodome and flat film devices with a top TCO layer is better than those without a top TCO layer, respectively. This is because TCO has a lower refractive index than a-Si:H so that light reflection is lower for the samples with the top TCO layers. However, this TCO enhancement effect is much less for nanodome devices (from 87 % to 94 %) than for flat film devices (from 48 % to 65 %), which indicates that the nanodome geometry without TCO already has very good antireflection property compared to the flat film geometry.

Third, for the short wavelength region (below 500 nm), all the light loss can be attributed to the light reflection since its absorption depth (∼100 nm) is smaller than the a-Si:H layer thickness of 280 nm. As seen in Figure 2a, without the top TCO coating, the absorption of nanodomes is always

above 85 %, while the flat one is below 60 %. Adding the TCO coating will improve the absorption above 88 % and 65 % correspondingly.

Fourth, for the long wavelength above 550 nm, significant interference oscillations appear in flat film devices while nanodome devices still show relatively flat broad band adsorption. The observed oscillations in flat film devices are basically Fabry—Perot interference, arising from the long wavelength light not absorbed by the a-Si:H layer interfering with the reflected light from the top layer of the device. For flat films without the top TCO layer, it causes a significant absorption valley at the region around 570, 640, and 750 nm. About 80 % of light escapes at the wavelength of 640 nm. While addition of the TCO layer reduces the reflection loss, it also shifts the absorption valleys to the shorter wavelengths, consistent with the light interference. The interference oscillations are greatly reduced for the nanodome devices, suggesting that very little light escapes after reflection by the Ag and thus their absence suggests significant light trapping effects.

Fifth, the most significant absorption improvement using the nanodome geometry versus the flat film one is in the wavelength range of 700—800 nm. a-Si:H has a band gap ∼710 nm and a long band tail. The absorption coefficient drops quickly when the light wavelength is above ∼700 nm. For flat film devices with the top TCO layer, there is a significant reduction of absorption down to 50 % while nanodome devices with the top TCO layer maintain absorption of ∼90 %. The relative improvement is ∼80 %. These data suggest that nanodomes can enhance light trapping significantly even for the absorption of photons below the band gap. However, it is hard to conclude at this moment whether all the absorption in this sub-band-gap wavelength range contributed to short-circuit current.

The exciting light absorption data of nanodomes result from their unique geometry, effective for antireflection and absorption enhancement. The antireflection effect is due to the tapered shape of nanodome structures with better effective refractive index matching with air. Previously, nanocone-shaped structures have been shown to have a refractive index matching with air that suppresses light reflection significantly.[10—14] Our nanodomes also offer such a mechanism to couple light into the a-Si:H layer with suppressed reflection. More excitingly, nanodomes can scatter light along the in-plane dimension, which enhances the light traveling path for absorption, providing a light trapping mechanism. Compared with the Lambertian scattering, which is based on well-understood surface texturing using features much larger than light wavelengths for efficient absorption enhancement effects,[26,27] our devices use subwavelength nanodome structures, which are more feasible for solar cells with only submicrometer thick absorber layers.[18] In addition, Ag reflectors have nanoscale modulations, which cause strong light scattering. Ag nanoparticles arrays have been widely incorporated for absorption en-
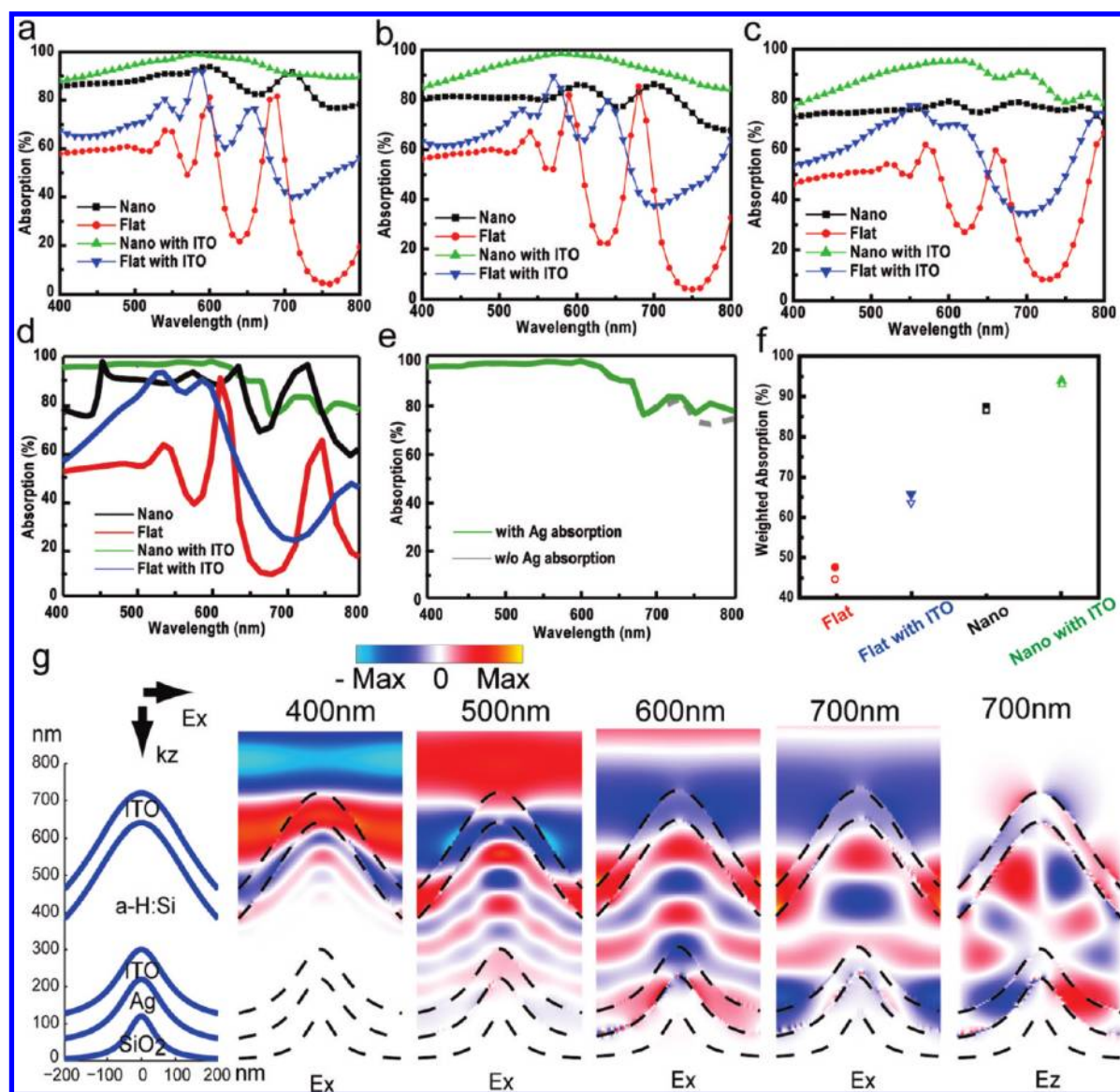
FIGURE 2. Light absorption measurement and simulation. (a−c) Integrating sphere measurement results of absorption under normal incidence (a): 30° angle of incidence (b), 60° angle of incidence (c). The samples are flat substrates without ITO coating (red), flat substrates with ITO coating (blue), nanodomes without ITO coating (black), nanodomes with ITO coating (green). (d) FTDT simulation of light absorption for flat and nanodome devices with and without ITO. (e) Simulation of absorption spectra for the case with (green) and without (dashed gray) Ag absorption loss. (f) The weighted absorption integrated over the wavelengths of 400−800 nm by experiment (solid symbols) and simulation (hollow symbols). (g) Snapshots of simulated electric fields in the structure for different wavelengths.

hancement in the region close to band gap edge in a variety of devices.[17−20] In those studies, the main mechanisms have been believed to be the large resonant scattering cross section of these particles. However, since these nanoparticles are put on top of the surface, part of the short wavelength light around resonant frequency is wasted by either scattering or absorption. In our nanodome devices, the nanostructured Ag back-reflector as bottom contact is a better choice: while long wavelength lights are strongly scattered by the modulated Ag back-reflector, the performance of short wavelength absorption is not compromised since significant absorption occurs through single path of the absorber before reaching the Ag films.

To elucidate the physical mechanisms involved in the efficiency enhancement, we have performed simulations by solving the Maxwell equations with three-dimensional finite-difference time-domain simulation[28] on the experimental device geometry. The cross section of the structure is shown in Figure 2g (left) with incident plane waves polarized in the x direction. The period of the nanodome array is 450 nm. The dielectric constants of silver and silicon are taken from tabulated experimental data modeled by complex-conjugate pole-residue method.[29] The simulated nanodome structure, can absorb 93% of normally incident sunlight for the spectral range from 400 to 800 nm (Figure 2d green curve and 2f green triangle), which matches well with experimen-

tal data (Figure 2a and f). The broad band absorption comes from two contributions. First, the reflection is greatly suppressed by the nanodomes. Such shape forms a graded refractive index profile, creating a broad band antireflection layer. For short wavelength around 400−500 nm (Figure 2g, E_x simulation for 400 and 500 nm), a-Si:H silicon is highly absorptive. Thus, with efficient antireflection effects, all the incident lights are absorbed in a single path through the silicon layer. Second, the nanodome shape can also efficiently couple the incident light into modes that are guided in the a-Si:H layer. (We note that the dispersion relation of such modes can be strongly influenced by the presence of plasmonic response of the Ag film.) This is particularly important for the long wavelength regime (Figure 2g, E_x simulation for 600 and 700 nm) where a-Si:H is less absorptive and a single path cannot absorb all the incident light. Figure 2g E_z simulation for 700 nm shows the z component of the electric field, indicating strong guided modes confined inside the nanodome structure. To evaluate the absorption loss by silver, we perform a separate simulation using a lossless silver model. Figure 2e shows the absorption spectra with (green line) and without (gray line) metal loss. For the lossless silver case, the weighted absorption for normal incident sunlight is 92 % as compared to 93 % for the realistic silver case. Therefore, the metal loss contributes only about 1 % of absorption.

For solar cells in a practical environment where sunlight can be quite diffuse, it is important to evaluate the absorption efficiency over a wide range of incident angles. Parts b and c of Figure 2 show the absorption measurement at incident angles of 30° and 60°, respectively. As the incident angle increases from 0 to 60°, the absorption over the whole spectrum for nanodome devices decreases only by 5 % while flat devices decrease by 13 %. These data suggest that nanodome devices have an advantage over flat film devices in the real environment. Indeed, nanodome and flat film devices look very different even to the eyes. Figure 3a shows photographs of nanodomes (left) and flat films (right) without the top TCO layers in diffuse light conditions, respectively. The flat film devices are mirror-like, highly reflective, and look red because of inefficient light absorption at the long wavelength while nanodome devices look black, due to efficient antireflection and light trapping.

To prove how effectively antireflection and light trapping can improve the power conversion efficiency of solar cells, we have tested nanodome and flat film solar cell devices in a solar simulator with 1 sun AM1.5G illumination. Excitingly, the nanodome devices show power conversion efficiencies that are 25 % higher than the flat film devices, made under otherwise identical conditions. An example is shown in Figure 3b, in which the nanodome device exhibits a power efficiency of 5.9 % (open circuit voltage, V_{oc} = 0.75 V; short circuit current, J_{sc} = 17.5 mA/cm²; fill factor, FF = 0.45) while the flat device exhibits an efficiency of 4.7 % (V_{oc} =0.76 V,
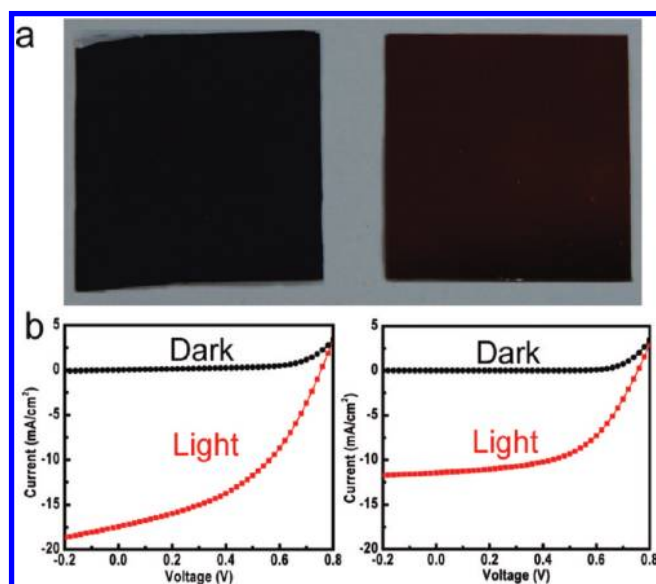

FIGURE 3. Power conversion of a-Si:H nanodome solar cells. (a) Photographs of nanodome solar cells (left) and flat film solar cells (right). (b) Dark and light $I−V$ curve of solar cell devices for nanodomes (left) and flat substrates (right).

J_{sc} =11.4 mA/cm², FF = 0.54). The significant improvement of power efficiency comes from a large short-circuit current of nanodome devices (17.5 mA/cm²) which is higher than that (15.6 mA/cm²) of the world record single junction a-Si:H solar cells with substrate configuration[22] with initial power efficiency of 10.6 %. The short-circuit current of nanodome devices is only slightly lower than the theoretical value (20.5 mA/cm²)[23] limited by the band gap. We believe that we can improve the efficiency of nanodome devices in the future by improving the open circuit voltage and fill factor via better materials deposition.

When solar cells are operated in real environments, dust particles accumulate on the solar cell surface over time, blocking the sunlight and thus reducing the power efficiency. To avoid the problem, integrating a self-cleaning function into the solar cells is desirable. Surface superhydrophobicity is known to offer such a self-cleaning capability.[30] Surfaces with very high water contact angles, larger than ~150° in particular, are called superhydrophobic surfaces. Although a flat surface can be modified to become hydrophobic with contact angles typically <120°, it is necessary to have nanoscale roughness to generate superhydrophobicity, which has been observed in nature on lotus leaves. Here we show that our nanodome solar cells possess the self-cleaning capability via superhydrophobicity due to the nanodome morphology. We have modified the surface of nanodome solar cells with hydrophobic molecules: perfluorooctyl trichlorosilane (PFOS). After modification, nanodomes are nearly superhydrophobic with high water contact angles (141° ± 2°) (Figure 4a). We found that such a high contact angle is adequate to realize a self-cleaning function. Nanodome solar cells accumulating a large amount of dust (Figure 4b) with
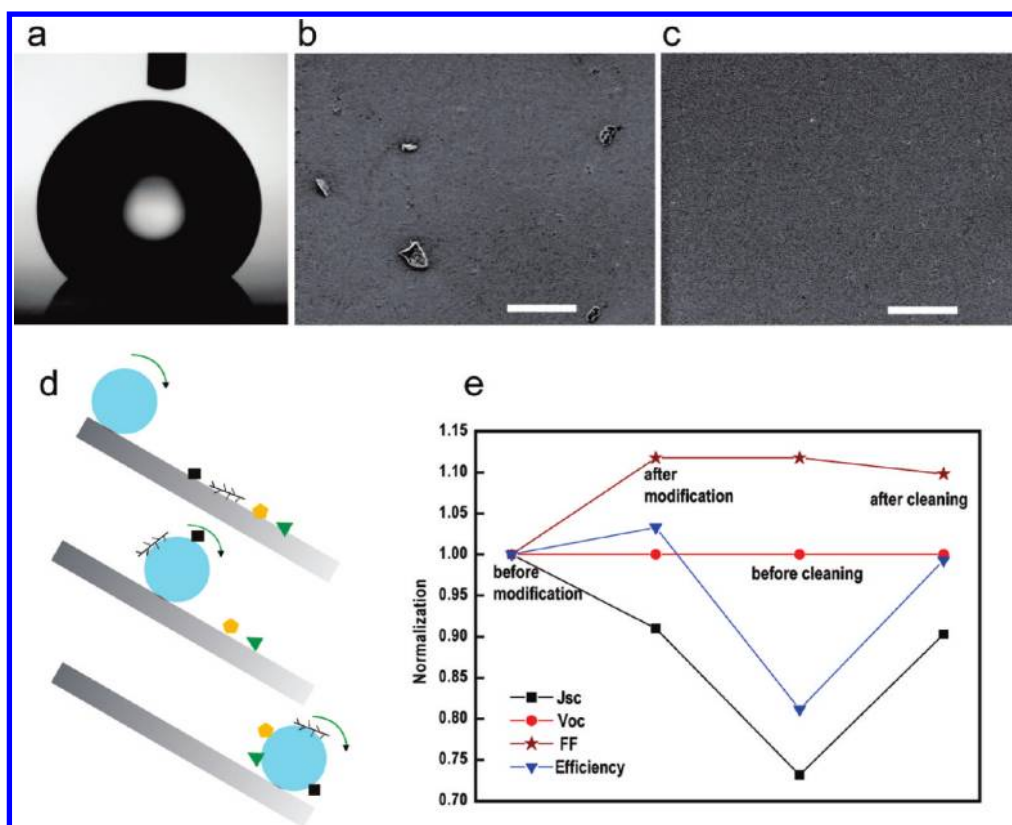
FIGURE 4. Self-cleaning of a-Si:H nanodome solar cells. (a) Optical micrograph of a drop of water on the nanodome solar cell surface after PFOS modification showing a large contact angle of 141°. **(b)** SEM of nanodome solar cells with dust particles, Scale bar 10 μm. **(c)** SEM of nanodome solar cells after water cleaning. Scale bar 10 μm. **(d)** Schematic showing the self-cleaning mechanism. **(e)** Change of FF, J_{sc}, V_{oc} and power efficiency during a cycle of the self-cleaning process.

different sizes and shapes can be cleaned up by simply rolling a water droplet across the surface (Figure 4d). After cleaning, nanodome solar cells were inspected under SEM and the dust particles were found to be removed Figure 4c. Figure 4e shows the device performance measured on the same nanodome device during each of the four step processes: step 1 before PFOS surface modification, step 2 after PFOS surface modification, step 3 adding dust particles, step 4 after water self-cleaning. The vertical axis refers to normalized data for the solar cell device performance parameters. From step 1 to 2, even though the FF and J_{sc}, show some changes due to mechanisms which are not yet clear, the power efficiency remain nearly the same. From step 2 to 3, the power efficiency drops significantly by 20% due to the low J_{sc} caused by light blocking of dust particles. From step 3 to 4, the self-cleaning process removes the dust particles and recovers the value of power efficiency. V_{oc} remains the same during the whole process.

In conclusion, we have demonstrated novel nanodome solar cell devices with effective antireflection and light trapping over a broad spectral range and a wide set of incidence angles, which leads to much higher power efficiency than that of the flat film devices. The nanoscale morphology of such solar cells also enables a self-cleaning function although the strategy on how to utilize it in practical environment requires future study. Our results open up exciting opportunities for improving the efficiency, reducing the materials usage and maintenance for a variety of solar cell technologies.

Materials and Methods. *Particle Synthesis and Assembly.* Monodisperse SiO$_2$ nanoparticles with diameters from 50 to 800 nm were produced by a modified Stober synthesis. These nanoparticles were then modified with aminopropyl methyldiethoxysilane so that they can be terminated with positively charged amine groups to prevent aggregation. Finally, they were assembled into closed-packed layers on substrates via the Langmuir–Blodgett method. More details can be found in our previous paper.[13,25]

Substrate Fabrication. Fluorine-based reactive ion etching was performed in an Applied Materials Technologies 8100 Hexode plasma etcher, operating with maximal rf power 1600 W and dc bias −530 V. Nanoscale cone-shape structures were made with a mixture of O$_2$ and CHF$_3$, flow rates ranging from 6 to 30 sccm and from 50 to 85 sccm, respectively. The etching rate can be tuned by power, chamber pressure, and reactive gases ratio with approximately 35 nm/min (±30% deviation). Aspect ratios and spacings between nanodomes can be determined by adjusting original particle sizes and etching conditions. In our study, nanoparticles with diameter about 450 nm were used,

which produced periodicity with similar scale. The etching corresponding to the shown device was performed with gas flow rates of O_2 at 6 sccm and CHF_3 at 85 sccm, respectively. The base pressure remained at 0.8 mTorr during the entire process.

Optical Measurements. Standard hemispherical measurements were carried out with an integrating sphere (Newport). A xenon lamp coupled to a monochromator was used for both wavelength-dependent and incident-angle-dependent measurements. The sample was mounted at the center of the sphere. The reflected light and transmitted light from the sample were uniformly scattered by the integrating sphere and collected by a photodetector. In this study, all light reflected from and transmitted through the sample was accounted, so this can be considered a measurement of the absolute absorption.

Hydrogenated Amorphous Silicon Deposition. The amorphous silicon doped and undoped layers were deposited by plasma enhanced chemical vapor deposition (PECVD) at 250 °C. A SiH_4 and H_2 gas mixture was used for intrinsic layer growth. CH_4 and B_2H_6 were added in for p-layer growth, while PH_3 was used as the dopant gas for n-layer growth. All the films contain a bonded hydrogen concentration around 10 atom %, to reduce the broadening of the conduction and valence band tails as well as the occurrence of dangling bonds.

Surface Modification. Perfluorooctyl trichlorosilane (PFOS) purchased from VWR International LLC was dissolved in hexane with a concentration of 10 mM. The a-Si:H device was immersed in the solution for 30 min followed by rinsing with hexane and blown dry with N_2. The contact angle was measured with the 3° camera look down method to help find baselines. We performed nonspherical mode to fit the droplet shape with ±1° uncertainty.

REFERENCES AND NOTES

(1) Gratzel, M. *Nature* **2001**, *414*, 338–344.
(2) Huynh, W. U.; Dittmer, J. J.; Alivisatos, A. P. *Science* **2002**, *295*, 2425–2427.
(3) Law, M.; Greene, L. E.; Johnson, J. C.; Saykally, R.; Yang, P. *Nat. Mater.* **2005**, *4*, 455–459.
(4) Luque, A.; Marti, A.; Nozik, A. J. *MRS Bull.* **2007**, *32*, 236–241.
(5) Tian, B.; Zheng, X.; Kempa, T. J.; Fang, Y.; Yu, N.; Yu, G.; Huang, J.; Lieber, C. M. *Nature* **2007**, *449*, 885–889.
(6) Kayes, B. M.; Atwater, H. A.; Lewis, N. S. *J. Appl. Phys.* **2005**, *97*, 114302.
(7) Ferry, V. E.; Sweatlock, L. A.; Pacifici, D.; Atwater, H. A. *Nano Lett.* **2008**, *8*, 4391–4397.
(8) *High Efficiency Silicon Solar Cells*; Green, M. A., Ed.; Trans Tech Publications: Brookfield, VT, 1987.
(9) Xi, J. Q.; Schubert, M. F.; Kim, J. K.; Schubert, E. F.; Chen, M.; Lin, S.-Y.; Liu, W.; Smart, J. A. *Nat. Photonics* **2007**, *1*, 176–179.
(10) Huang, Y.-F.; Chattopadhyay, S.; Jen, Y.-J.; Peng, C.-Y.; Liu, T.-A.; Hsu, Y.-K.; Pan, C.-L.; Lo, H.-C.; Hsu, C.-H.; Chang, Y.-H.; Lee, C.-S.; Chen, K.-H.; Chen, L.-C. *Nat. Nanotechnol.* **2007**, *2*, 770–774.
(11) Lee, Y. J.; Ruby, D. S.; Peters, D. W.; McKenzie, B. B.; Hsu, J. W. P. *Nano Lett.* **2008**, *8*, 1501–1505.
(12) Lohmuller, T.; Helgert, M.; Sundermann, M.; Brunner, R.; Spatz, J. P. *Nano Lett.* **2008**, *8*, 1429–1433.
(13) Zhu, J.; Yu, Z.; Burkhard, G. F.; Hsu, C.-M.; Connor, S. T.; Xu, Y.; Wang, Q.; McGehee, M.; Fan, S.; Cui, Y. *Nano Lett.* **2009**, *9*, 279–392.
(14) Yu, Z.; Gao, H.; Wu, H.; Ge, H.; Chou, S. Y. *J. Vac. Sci. Technol., B* **2003**, *21*, 3974–3977.
(15) Fang, H.; Li, X.; Song, S.; Xu, Y.; Zhu, J. *Nanotechnology* **2008**, *19*, 255703.
(16) Barnes, W. L.; Dereux, A.; Ebbesen, T. W. *Nature* **2003**, *424*, 824–830.
(17) Barry, P. R.; Peter, P.; Stephen, R. F. *J. Appl. Phys.* **2004**, *96*, 7519–7526.
(18) Catchpole, K. R.; Polman, A. *Opt. Express* **2008**, *16*, 21793–21800.
(19) Derkacs, D.; Lim, S. H.; Matheu, P.; Mar, W.; Yu, E. T. *Appl. Phys. Lett.* **2006**, *89*, No. 093103.
(20) Nakayama, K.; Tanabe, K.; Atwater, A. *Appl. Phys. Lett.* **2008**, *93*, 121904.
(21) Pillai, S.; Catchpole, K. R.; Trupke, T.; Green, M. A. *J. Appl. Phys.* **2007**, *101*, No. 093105.
(22) Yang, J. C. *Prog. Photovoltaics* **1998**, *6*, 181–186.
(23) Shah, A. V.; Schade, H.; Vanecek, M.; Meier, J.; Vallat-Sauvain, E.; Wyrsch, N.; Kroll, U.; Droz, C.; Bailat, J. *Prog. Photovoltaics* **2004**, *12*, 113–142.
(24) Schropp, R. E. I., Zeman, M. *Amorphous and Microcrystalline Silicon Solar Cells: Modeling, Materials, and Device Technology*; Kluwer Academic Publishers: Boston, MA, 1998.
(25) Hsu, C.-M.; Connor, S. T.; Tang, M. X.; Cui, Y. *Appl. Phys. Lett.* **2008**, *93*, 133109.
(26) Mutitu, J. G.; Shi, S.; Chen, C.; Creazzo, T.; Barnett, A.; Honsberg, C.; Prather, D. W. *Opt. Express* **2008**, *16*, 15238–15248.
(27) Tiedje, T.; Yablonovitch, E.; Cody, G. D.; Brooks, B. G. *IEEE Trans. Electron Devices* **1984**, *31*, 711–716.
(28) Taflove, A.; Hagness, S. *The Finite-Difference Time-Domain Method*; Artech House: Boston, MA, 2005.
(29) Han, M.; Dutton, R. W.; Fan, S. *IEEE Microwave Wireless Compon. Lett.* **2006**, *16*, 119–121.
(30) Genzer, J.; Marmur, A. *MRS Bull.* **2008**, *33*, 742–746.